International Journal of Nanomedicine

Dovepress
Taylor & Francis Group

Open Access Full Text Article

ORIGINAL RESEARCH

Gas Vesicle-Assisted Ultrasound Imaging for Effective Anti-Tumour CAR-T Cell Immunotherapy Efficacy in Mice Model

Yizhen Huang[1,2,*], Zhao Yin[3,*], Renhao Xu[2,*], Wenyi Zheng[2], Qing Zhang[3], Meijun Zhou[2], Zhili Xu[2], Yanni He[2,4], Shuang Liu[3,4], Hongmei Liu[1,2,4]

[1]The Second School of Clinical Medicine, Southern Medical University, Guangzhou, 510515, People's Republic of China; [2]Department of Ultrasound, Institute of Ultrasound in Musculoskeletal Sports Medicine, The Affiliated Guangdong Second Provincial General Hospital of Jinan University, Guangzhou, 510317, People's Republic of China; [3]Department of Hematology, The Affiliated Guangdong Second Provincial General Hospital of Jinan University, Guangzhou, 510317, People's Republic of China; [4]Guangdong Engineering Technology Research Center of Emergency Medicine, Guangzhou, 510317, People's Republic of China

*These authors contributed equally to this work

Correspondence: Hongmei Liu; Shuang Liu, Email liuhm@gd2h.org.cn; liush@gd2h.org.cn

Introduction: Real-time tracking of Chimeric Antigen Receptor (CAR) T cell trafficking provides crucial information regarding the targeted migration, infiltration, and persistence of CAR-T cells within the tumour microenvironment (TME). This information is invaluable for the timely adjustment of auxiliary treatment strategies in clinical settings.

Methods: We designed a gas vesicles (GVs)-labeled CAR-T (GVs@CAR-T) complex using nanoscale GVs with excellent ultrasound reflectivity to label CAR-T cells for post-labelling ultrasound molecular imaging.

Results: GVs@CAR-T complexes achieved stable ultrasound imaging for up to five days. In vitro and vivo experiments demonstrated that GVs labelling did not affect the anti-tumour function of CAR-T cells. In a subcutaneous tumour model, ultrasound molecular imaging was used to monitor the targeted migration of systemically infused GVs@CAR-T cells, which revealed a positive correlation between specific infiltration and therapeutic efficacy.

Conclusion: This study presents an efficient method for in vivo tracking of CAR-T cells and offers new insights for predicting the efficacy of CAR-T cell immunotherapy.

Keywords: cell tracking, CAR-T therapy, ultrasound imaging, nanobubbles

Introduction

Chimeric Antigen Receptor (CAR) T cell therapy represents a groundbreaking advancement in cancer treatment.[1–3] By targeting genetically-engineered, live T-cells, this therapeutic approach facilitates durable clinical anti-tumour effects.[4–7] Several CAR-T cell therapies, such as Kymriah, Tecartus, and Liso-cel, have been approved for treating relapsed or refractory B-cell leukaemia and lymphoma.[8–10] The key to the success of CAR-T cell therapy lies in its ability to effectively infiltrate tumour sites.[11,12] However, due to tumour heterogeneity and individual patient differences, the efficacy of CAR-T cell therapy can vary significantly.[13] Timely prediction and assessment of CAR-T efficacy are of great clinical significance.[14–16] Recent clinical studies have also indicated that 10%–20% of patients receiving CAR-T therapy experience no response or disease progression.[17] Notably, the degree of CAR-T cell homing observed in tumour biopsies shows a significant positive correlation with treatment response.[9] If real-time tracking of CAR-T cell homing can provide information on targeted migration, infiltration, and persistence in the tumour microenvironment (TME),[18,19] it would considerably aid the timely supplementation of supportive treatment strategies, significantly impacting the clinical success of CAR-T therapy.

Received: 19 December 2024
Accepted: 2 April 2025
Published: 16 April 2025

In recent years, significant efforts have focused on developing imaging strategies that integrate advanced materials for adoptive cell tracking.[20,21] Various methods, including s nuclear medicine imaging and magnetic resonance imaging, have been utilized for this purpose.[22–24] Different modalities have contributed new insights to the field of adoptive cells. Scholars such as Wei et al utilised MegaPro-NP-labelled CAR-T, allowing the detection of CAR-T cell homing through Magnetic Particle Imaging (MPI) imaging technology.[25] However, because MPI requires magnetic field variations to obtain signals, this process involves relatively long imaging times.[26] Additionally, data acquisition and reconstruction algorithms require processing time, limiting real-time imaging and thereby imposing certain constraints on the evaluation of CAR-T efficacy. Shao et al employed radionuclide non-invasive imaging to achieve high sensitivity and precision in visualizing CART cells in vivo.[27] However, the high levels of radioactivity involved can impair the viability of cells.[28] In contrast, ultrasound molecular imaging offers advantages such as real-time dynamics, no radiation, and rapid image acquisition, making it widely used in clinical research.[29] Furthermore, the use of ultrasound contrast agents (UCAs) produces ideal contrast in ultrasound images, with microbubbles being commonly employed as contrast agents in ultrasound molecular imaging.[30,31] Many studies have shown that microbubble-based acoustic probes successfully achieve molecular targeted imaging of important markers such as VEGFR2, α(v)-β(3), and VACM-1.[32–34] However, there are still significant challenges in targeting tumour imaging, as traditional microbubbles, due to their relatively large size (typically 1–5 μm), cannot traverse tumour blood vessels and contact cells outside the tumour.[35,36] If existing ultrasound imaging technologies can be combined with ultrasound contrast agents of smaller size, it would become possible to achieve early prediction and assessment of CAR-T efficacy.[37]

In our previous study, we prepared hollow mesoporous organosilica nanoparticles (HMONs) loaded with perfluoropentane (PFP) to enable the visualisation of macrophage cell-based drug delivery systems, and real-time dynamic imaging of macrophages was achieved by the ultrasound-triggered phase transition of PFP.[38] To simplify the preparation of a visualisable cell–drug delivery system, the latest progress in this study employed more stable and easily prepared gas vesicles (GVs) extracted from Halobacterium NRC-1 (Halo),which were co-cultured with multifunctional mesenchymal stem cells (MSCs) to successfully obtain GV-labelled MSCs (GVs@MSCs). This allowed for targeted tracking of these labelled cells, demonstrating their functions in bone repair and anti-inflammation.[39] The GVs have a nanometre-sized hollow structure made of a biological protein shell, and the flexibility of this shell, which deforms under an acoustic field, is key to ensuring stability.[40–42] This deformation generates echoes at harmonic frequencies, allowing GVs to distinguish their echoes from biological tissues at primary frequencies.[43] Therefore, if GVs can be used to label CAR-T cells, it holds promise for achieving real-time, dynamic targeted ultrasound imaging tracking of CAR-T cells during in vivo therapeutic processes.

In this study, we successfully utilised GVs as acoustic markers to label CAR-T cells (GVs@CAR-T), enabling dynamic, real-time, and targeted homing tracing of labelled cells at target sites following systemic infusion through ultrasound contrast imaging. This complex not only demonstrated stable binding in vitro, achieving significant ultrasound imaging over a duration of up to 5 days, but also allowed the evaluation of the tumour-targeting specificity of CAR-T cells in vivo using ultrasound contrast imaging for homing tracing. Ultimately, this enables the prediction and assessment of therapeutic effects in lymphoma. Therefore, we developed an efficient tracing method for cell therapy using nanometre-sized biological bubbles, providing a new approach for predicting and evaluating the efficacy of CAR-T cell therapy.

Materials and Methods

The Isolation and Characterization of Gas Vesicles (GVs)

Bacterial culture and biosynthetic nanobubble isolation were performed as our previous report.[40] *Halo* were cultured in ATCC medium 2185 at 37 °C with shaking at 150 rpm for 7 days. Following this, *Halo* cultures were transferred to a separating funnel and allowed to sit at room temperature for two weeks. After floating, the Halo cells were separated, lysed using TMC buffer, and centrifuged at 350 ×*g* for 4 h. The resulting milky GVs were isolated and stored at 4 °C. The structure of the GVs was analysed using Scanning Electron Microscope (SEM) (HT7800, HITACHI, UK). Dynamic light scattering (DLS) was used to determine size distribution and zeta potential (Malvern-MS2000, Malvern, UK). Measurements were performed using a spectrophotometer (Nanodrop 2000c; Thermo Scientific, USA) at 500 nm to determine optical density (OD). The stability of the GVs in 1× PBS (pH 7.4) was evaluated by measuring the nanocomplex size using DLS for 7 days.

CAR-T Cell Generation

Human peripheral blood mononuclear cells (PBMCs) from healthy donors were used, and T cells were activated with anti-CD3 Dynabeads (ThermoFisher Scientific) at a cell-to-bead ratio of 1:3, 72 hours prior to transduction. CD19-CAR-T cells were produced by transducing donor T cells with a retroviral vector, following established protocols.[44] The purity of T cells is analyzed through flow cytometry (FACSAria III, BD, USA). After PBMC activation with DynaBeads (day 1) and retroviral transduction (day 4), CD19-CAR-T cells were harvested and Flow cytometry is used to detect the efficiency of Lentiviral infection. The human CAR-T cell cultured in X–VIVO 15 medium (Lonza) containing with 10% FBS (Gibco), 1% penicillin/streptomycin (Gibco) and 100U/mL recombinant human IL-2 (Elabscience). The study complies with the Declaration of *Helsinki* and was approved by the Ethics Committee of the Guangdong Second Provincial General Hospital (Ethical approval number 2022-XJS-SB-14). All PBMC donors provided written informed consent.

Evaluation of Cytotoxicity of Gas Vesicles Label CAR-T Cells (GVs@CAR-T) in vitro

Cell viability was assessed using a CCK-8 assay (Dojindo Laboratories) to determine the optimal GV concentration. 5×10^3 CAR-T cells per well) in a 96-well plate were treated with GVs at different concentrations (OD500) (0, 0.5, 0.75, 1, 1.25, 1.5, 1.75, and 2) for 12 h and measured using a Multimode Reader (SynergyH1, BioTek, USA) at OD 450 nm to evaluate cytotoxicity. 5×10^3 CAR-T cells per well) 96-well incubated with GVs (OD500) = 1.0 for 12 h, and then free GVs were removed.

The viability of GVs@CAR-T cells was tested using the CCK-8 assay (Dojindo Laboratory) on days 1, 2, 3, 4, and 5, respectively. CAR-T cells 5×10^5 CAR-T cells per well in six-well plates were added to GVs (OD500=1) for 12 h, and free GVs were removed. GVs@CAR-T cell apoptosis was measured using the Annexin V-PI Apoptosis Detection Kit (Elabscience) according to the manufacturer's instructions. Data were acquired using the FACS analyser (FACSAriaIII, BD, USA) and analysed using FlowJo™ software. The assay was performed in triplicates and repeated three times.

The Preparation and Characterization of GVs@CAR-T

CAR-T cells were incubated with GVs for 8 hours at 37 °C and free GVs was removed via PBS rinse, successfully constructing the labelled CAR-T cells (GVs@CAR-T). Transmission Electron Microscope (TEM) was used to determine the morphology and subcellular localisation of GVs in CAR-T cells (HT7800, HITACHI, UK). Labelling was performed by co-incubating 1.1′-bis(octadecyl)-3,3,3′,3′-tetramethylindocarbocyanine perchlorate (DiI) dye (Solarbio) with GVs (OD500=1). The labelled -GVs were incubated with CAR-T cells for 8 hours and then Hoechst 33342 dye (MCE) and 3.3′-Dioctadecyloxacarbocyanine perchlorate (DiO) dye (MCE) was used to stain the GVs@CAR-T, followed by assay with a confocal microscope (Leica Stellaris 5, Germany). To evaluate the uptake efficiency for CAR-T cells, labelled GVs were incubated with CAR-T cells for 0, 2, 4, 6, and 8 h, followed by flow cytometry (FACSAria III, BD, USA).

Contrast-Enhanced Ultrasound (CEUS) Imaging of GVs and GVs@CAR-T in vitro

We suspended 1 mL of GVs at different concentrations (OD500) of 0.5, 1, 1.5, and 2 in agarose phantom wells in triplicate. An equal volume of PBS was used as the control group. The GVs@CAR-T cells were collected from the culture plates and suspended at different density,5×10^4, 5×10^5, 5×10^6, 5×10^7, and 5×10^8 cells per well) into the agarose phantom wells in triplicate. CAR cells with similar cellular densities were used as controls. Each well containing 5×10^7 GVs@CAR-T was collected into agarose model wells, with three replicates, followed by continuous CEUS imaging on days 1, 3, 5, and 7. The experimental imaging equipment and parameters were as follows: Canon Aplio i800 imaging system (MI 0.02, contrast gain 30 dB, dynamic range 15 dB, and depth 20 mm) using an i18LX5 probe with a working frequency of 8 MHz. The contrast signal intensities were quantitatively analysed using the imaging system (Aplio i800, Canon, Japan).

In vitro Anti-Tumor Study of GVs@CAR-T

The effector cell CAR-T or GVs@CAR-T cells adjusted on the basis of transduction efficiency were co-cultured with the target cell Raji-Luc (1×10^4 per well) at E:T ratios of 8:1, 4:1, 2:1,1:1 for 24 h in 96-well U-bottom plates in triplicate. A PerkinElmer IVIS Spectrum Imaging System (PerkinElmer) was used to image the cells after adding 5 mg/mL D-luciferin (PerkinElmer) and incubating the cells for 5 min at 37 °C. Lactate Dehydrogenase (LDH) release cytotoxicity assays were performed using the CytoTox 96® Non-Radioactive Cytotoxicity Assay Kit (Promega, Madison, WI, USA)

following the manufacturer's protocol. The plating method was consistent with that described previously. This equation was used to calculate specific lysis: lysis (%) = [(effector-target cell mix -effector cell control)–low control)]/(high control-low control) × 100%. The assay was repeated thrice.

In vitro Cytokine Release Assays of GVs@CAR-T

For cytokine release assays, 1×10^5 CAR-T or GVs@CAR-T cells per well, adjusted on the basis of transduction efficiency, were cocultured with 1×10^5 cells per well in 24-well plates, and the supernatant was collected after 12 h for cytokine release assays using a Luminex human cytokine panel (EMD-Millipore). CAR-T the 1×10^5 per well CAR was adjusted based on transduction efficiency without cocultured with Raji cells and was used as the control group. The assay was performed in triplicates and repeated three times.

Impact of GVs on CAR-T Cell Activation Dynamics and Exhaustion Phenotypes

Each tube contained 1×10^5/mL GVs@CAR-T cells, which were then subjected to staining procedures with the following fluorescence-conjugated antibodies for 30 minutes at 4 °C: 1 μL of anti-CD3 (BioLegend) and anti-CD69 (BioLegend), and 1 μL of anti-CD3 (BioLegend) and anti-PD-1 (BioLegend), respectively. The same procedure was applied to the CAR-T cells as in the control group. Next, the cells were washed three times with PBS, and then resuspended in 1 mL of PBS for detection using flow cytometry (FACSAria III, BD, USA) and analysed using FlowJo™ software. The assay was performed in triplicates and repeated three times.

In vivo Studies Using Animal Model

Experimental procedures were carried out in accordance with the NIH Guide for the Care and Use of Laboratory Animals and were approved by the Institutional Animal Care and Use Committee (IACUC) of the Guangdong Second Provincial General Hospital Experimental Animal Center (Approval No. 2022-DW-KZ-093-01). Anaesthesia was induced with 3% isoflurane and maintained with 1% isoflurane during all animal procedures. Male NOD.Cg-PrkdcscidIl- 2rgtm1Wjl/SzJ (NSG) mice 6-week-old were used.

Raji cancer cells (1×10^6 cells/mouse) were injected into the backs of 6-week-old NSG mice (n=12) to establish subcutaneous tumours. After the formation of subcutaneous tumours, the mice were randomly divided into two groups: (a) CAR-T (1 × 107 transduced cells adjusted for transduction efficiency) (n=6) and (b) GVs@CAR-T (1×10^7 transduced cells adjusted for transduction efficiency) (n=6). Mice were intravenously administered GVs@CAR-T or CAR-T cells, and post-B-mode ultrasound and CEUS images were obtained 0, 24, 48 and 72 h post-injection at the tumour site. Three mice from each group were used. Before injection, GVs@CAR-T and CAR-T were incubated with DiI dye (Solarbio) for 30 min, after which the free DiI dye was removed. 48 hours after injection, the mice were sacrificed and their tumour tissues and major organs (heart, liver, spleen, kidney, and lungs) were imaged using IVIS imaging (Perkin Elmer, Waltham, MA, USA). IVIS.

Raji cancer cells (1×10^6 cells/mouse) or K562 cancer cells (1×10^6 cells/mouse) were injected into the backs of 6-week-old NSG mice (n=8) to develop subcutaneous CD19-positive (n=4) and CD19-negative (n=4) models, respectively. Each mouse model was intravenously injected with 1×10^7 transduced GVs@CAR-T cells. CEUS and parametric imaging were used to track the infiltration and homing of GVs@CAR-T cells in both tumour models. These imaging techniques were performed at the tumour site at 0.5, 12, 24, and 48-hours post-injection. In imaging procedures, 3% isoflurane was used for induction, and 1% isoflurane for maintenance of anaesthesia. Tumour growth was monitored using BLI 1 d pre-injection and 1, 2, and 3-days. Every 2–3 days, tumour sizes were measured using a digital caliper and computed using the following ellipsoidal formula: $V = (\text{width}^2 \times \text{length})/ 2$. According to the Animal Research Committee guidelines, mice with tumour volumes greater than 2500 mm^3 were euthanised.

Raji cancer cells (1×10^6 cells/mouse) were injected into the backs of 6-week-old NSG mice (n=18) to induce subcutaneous tumour development. The animals were randomly divided into two groups: (a) GVs@CAR-T (n=15) and (b) Mock-T (n=3), corresponding to the intravenous injection of (a)1×10^7 transduced cells adjusted on transduction efficiency GVs@CAR-T cells in 100 μL saline and (b) 1×10^7 Mock-T cells in 100 μL saline. Tumour growth was monitored by BLI, and ultrasound imaging was conducted on mice (a) and (b) before and 0.5, 12, 24, and 48 h after

injection. Every 2–3 days, tumour sizes were measured using a digital caliper and computed using the following ellipsoidal formula: V = (width^2 × length)/ 2. According to the Animal Research Committee guidelines, mice with tumour volumes greater than 2500 mm³ were euthanised. For in vivo toxicity assessment, blood samples were collected 32 days after treatment. Plasma was prepared from whole-blood samples collected by centrifugation. The serum levels of AST, ALT, BUN, and creatinine were determined using AST, ALT, BUN, and creatinine dry slide reagents with a DRI-CHEM 3500S chemistry analyser (Fujifilm, Japan). On day 32, all mice were euthanised and the major organs (kidneys, liver, lungs, heart, and spleen) were harvested for H&E staining.

Ultrasound Molecular Imaging in vivo

For in vivo imaging, ultrasound images were collected using a Vevo 3100 LAZR imaging system (Visual Sonics, Canada) equipped with an MX250 probe. The parameters were configured following the manufacturer's guidelines to minimise tissue background in vivo (frequency, 18 MHz; transmission power, 4%; Contrast Gain, 20 dB; Dynamic Range, 30 dB). The ultrasound images were exported, and MATLAB (MathWorks) was used to quantify the intensity values in the nonlinear contrast-mode images. Regions of interest (ROIs) were manually defined to cover the intratumoral volumes while avoiding tissue boundaries.

Statistical Analysis

All experiments in this study were performed at least in triplicate and repeated three times, and the data were expressed as mean ± S.D. GraphPad Prism 10.0 was used for statistical analysis. Statistical significance was defined as $P > 0.05$, not significant; $^*P < 0.05$, $^{**}P < 0.01$, and $^{***}P < 0.001$.

Results and Discussion

Characterization and Biocompatibility of GVs

GVs were first biosynthesized by Halo and then isolated. SEM images demonstrated that the GVs possessed a uniform, rugby-shaped morphology (Figure 1A). The prepared GVs had an average particle size of 272.96 ± 6.18 nm and a zeta potential of –32.4 ± 3.2 mV (Figure 1B and C), which is stable in PBS for one week (Figure 1D), demonstrating excellent stability of the nanocomplexes in vitro. The GVs particle size is smaller than that of traditional acoustic contrast agents, and the nanoscale size facilitates passage through the tumour vasculature and interaction with extracellular tumour cells.[45,46] Furthermore, as the concentration of GVs increases, the ultrasound imaging quality also improves (Figure 1E). However, due to the phenomenon of backscatter at excessively high concentrations (OD 500) ≥ 2 the imaging quality becomes poorer instead. Quantitatively, concentrations of GVs (OD500) = 0.5, 1.0, 1.5, and 2.0, showed 95.76-, 768.12-, 826.90-, and 594.60-fold higher acoustic signal intensities, respectively, than PBS (Supplementary Figure 1).

The primary human T cells were isolated from the Peripheral Blood Mononuclear Cells (PBMC) and identified by flow cytometry with a purity of ~99% (Supplementary Figure 2A) The anti-CD19 CAR construct included an anti-CD19 single-chain variable fragment, a CD8α hinge domain, a CD28 transmembrane domain, a 4–1BB cytoplasmic domain, and a CD3ζ cytoplasmic domain.[47] The T cells were then transfected with CAR Lentivirus and assessed the infection rate to be 66.2% (Supplementary Figure 2B). To determine the biocompatibility of the GVs, haemolysis, cytotoxicity, and apoptosis assays were performed. As shown in Figure 1F, the positive control group exhibited haemolysis, whereas the GVs tubes, similar to the negative control group, showed no haemolysis of erythrocytes. The cytotoxicity results indicated that the viability of CAR-T cells was slightly decreased at a GVs concentration of OD500 = 2 ($P < 0.05$) (Figure 1G). The CCK-8 assay and flow cytometry revealed no significant differences in viability and long-term proliferation between GVs@CAR-T and non-labelled CAR-T cells (Figure 1H, Supplementary Figures 3 and 4), indicating that GVs did not adversely affect apoptotic activity or cell death levels.

Validation of the Ultrasound Imaging Performance of GVs@CAR-T in vitro

To evaluate the ultrasound-contrast imaging ability of GVs@CAR-T cells in vitro, we suspended varying numbers of GVs@CAR-T cells in agarose phantom wells. CEUS revealed labelled CAR-T cells that had a certain level of signal

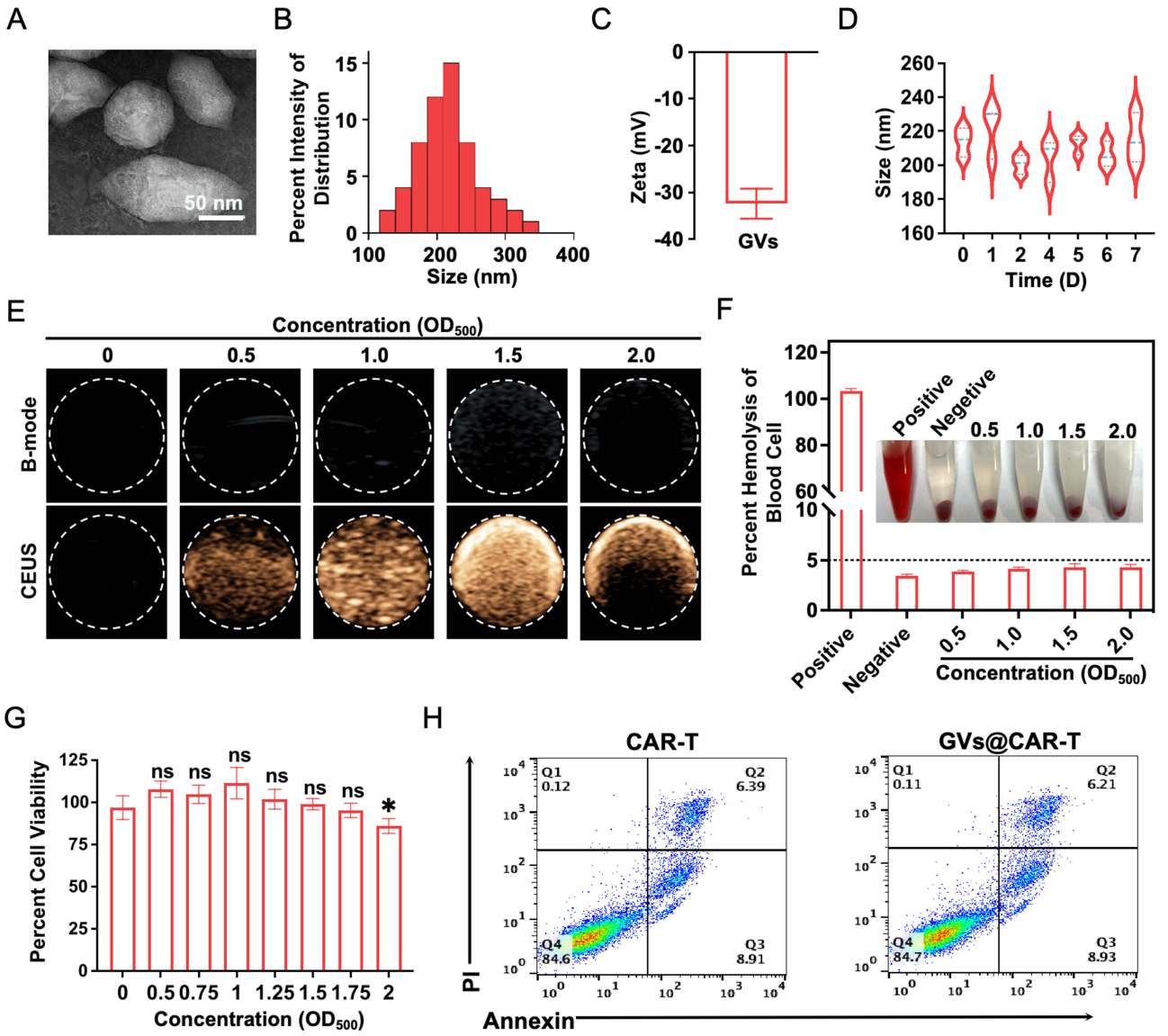

Figure 1 Characterization and Biocompatibility of GVs. (**A**) Representative SEM images of the GVs. Scale bar, 50 μm. (**B**) Particle size distribution of the GVs. (**C**) The average electric potential (mV) of GVs assessed by ZetaView. (**D**) The size stability of GVs in 1 × PBS buffer (pH 7.4) for 7 days. (**E**) Representative ultrasound images of GVs at different concentrations In vitro in both B-mode (upper) and CEUS mode (lower). (**F**) Images of erythrocytes in PBS (2%) mixed with GVs. PBS and dH_2O were negative and positive control, respectively (n=3). (**G**) Viability of CAR-T cells treated with GVs for 12 hours at a range of concentrations (n=3). (**H**) Percentages of Annexin V+ cells in the CAR-T and GVs@CAR-T (n=3). ns, not significant, *P <0.05.

starting at 5×10^5 cells/mL. At 5×10^6 cells/mL, the cells were distinguishable from the background (Figure 2A). GVs@CAR-T cells exhibited heightened acoustic signals, and the contrast increased with cell concentration, peaking at 5×10^8 cells. Despite a density of up to 5×10^6 cells/mL, the unlabelled CAR-T cell group did not exhibit any signal. The signal intensities of CEUS images were quantified (Figure 2B). There was a 13.44-fold enhancement in labelled CAR-T cells compared to that in non-labelled CAR-T cells at 5×10^5 cells/mL, revealing a detection threshold of approximately 5×10^5 cells/mL. To verify that the signal intensities in the CEUS images were due to the successful labelling of CAR-T cells with GVs, we performed confocal microscopy and found that GVs were taken up by the CAR-T cells (Figure 2C). To determine whether GVs reside within CAR-T cells or are bound to their surfaces, we examined their locations. TEM revealed that the GVs were located within the cytoplasm of CAR-T cells (Figure 2D and Supplementary Figure 5). Thus, GVs can efficiently label CAR-T cells in vitro. To further assess the CAR-T labelling efficiency, we used flow cytometry for detection. The results revealed that with increasing incubation time with GVs, the labelling rate of CAR-T cells also

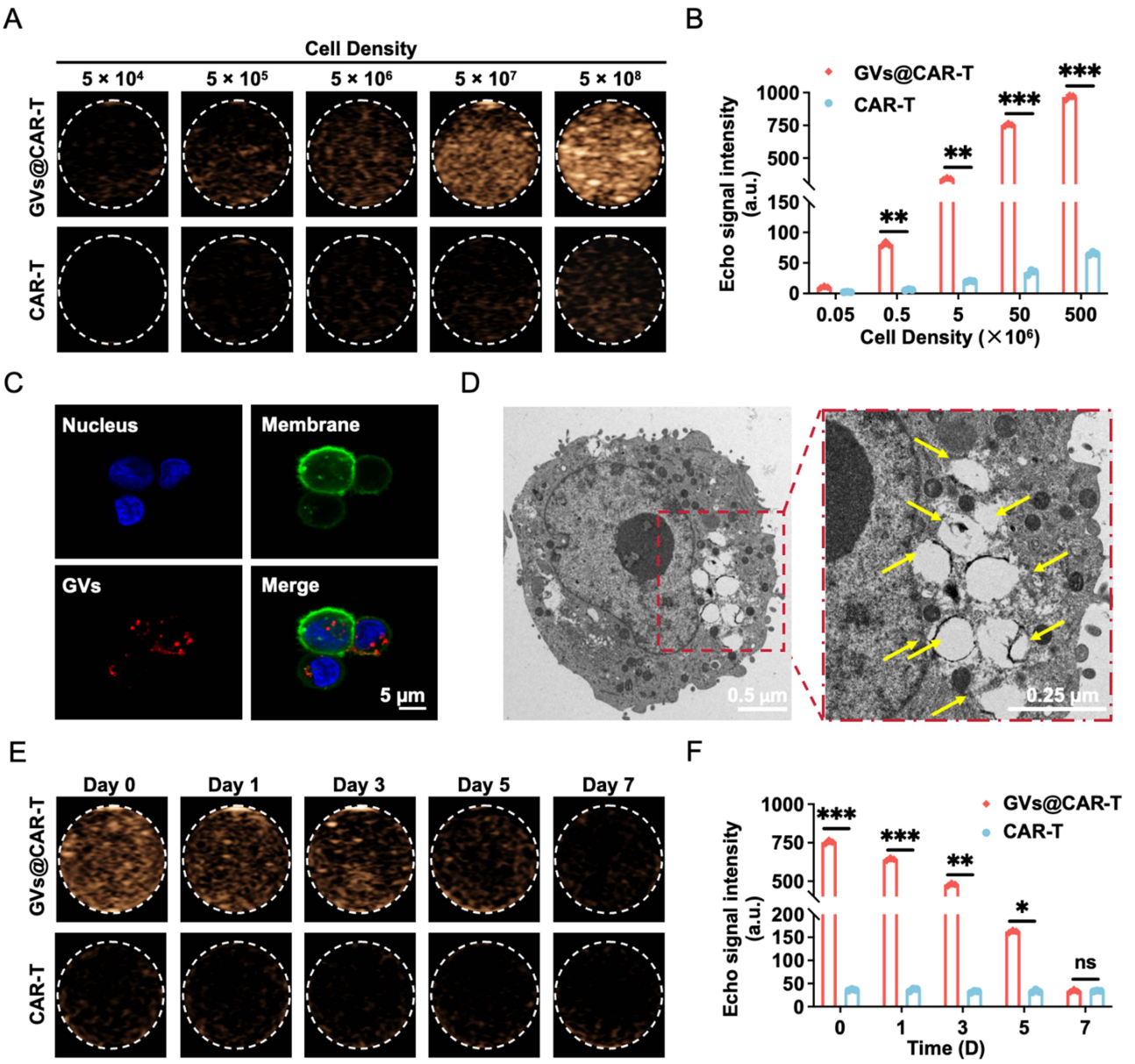

Figure 2 In vitro GVs@CAR-T exhibiting perfect ultrasonic imaging capability. (**A**) Representative CEUS images and (**B**) quantified CEUS intensity of GVs@CAR-T and CAR-T at concentrations of 5 × 10^4, 5 × 10^5, 5 × 10^6, 5×10^7 and 5×10^8. (**C**) Representative confocal laser scanning microscope images of GVs@CAR-T. Hoechst, nucleus; DiO, membrane; DiI, GVs. Scale bar, 5 μm. (**D**) Representative TEM image of GVs@CAR-T. The yellow arrows indicate GVs. Scale bars, 0.5μm for lower magnification, 0.25 μm for higher magnification. (**E**) Representative In vitro CEUS image and (**F**) Quantified CEUS intensity of 5×107 GVs@CAR-T and CAR-T on day 0, 1, 3, 5 and 7. ns, not significant, **P* <0.05, ***P* < 0.01, and ****P* < 0.001.

increased, reaching 99.9% at 8 h without the use of chemical or mechanical operations (Supplementary Figure 6). These findings indicate that labelling with GVs enhances the specific identification of target cells in biological tissues, as shown in previous studies.[48]

To assess the long-term tracking of CAR-T cells in a therapeutic context, we further examined the duration of the CEUS signal following GV labelling of CAR-T cells. Labelled cells were imaged at various post-labelling incubation times (Figure 2E) and maintained at a consistent density.[43] Despite the decline in signal intensity over extended incubation periods, the labelled cells could still be clearly differentiated from non-labelled cells, even after 5 days (Figure 2F). This in vitro signal loss can be attributed to two factors. First, while cells were resuspended at the same density at each time point, cell proliferation during the extended incubation period could reduce labelling rates, as the total number of GVs remained constant while cell numbers increased.[43] Secondly, interactions between cells and GVs

https://doi.org/10.2147/IJN.S508846

may also play a role in the reduction of ultrasound signal over time.[48] The stability of the observed signal over a 5-day period is sufficient for tracking CAR-T cells during the early phase, as they are expected to begin tumour infiltration shortly after infusion.[49] In summary, GVs@CAR-T demonstrating robust and stable in vitro imaging capabilities and laying the groundwork for high-quality in vivo imaging.

CEUS Imaging Enabled Spatiotemporal Tracking of GVs@CAR-T in Tumour-Bearing Mice

The tumour-killing capacity of CAR-T cells is a pivotal factor in their effectiveness as a cancer treatment.[50] Therefore, it is essential to evaluate the tumour-killing function of GVs@CAR-T cells before employing CEUS imaging for in vivo tracking. Our in vitro experiments demonstrated that GVs@CAR-T cells exhibited a dose-dependent tumour-killing effect against Raji-Luc cells, as evidenced by luminescence-based (Figure 3A) and LDH cytotoxicity assays (Figure 3B). Importantly, no statistically significant differences in cytotoxicity efficiency were observed between the GVs@CAR-T and CAR-T groups at effector-to-target ratios of 8:1, 4:1, 2:1, and 1:1 ($P > 0.05$). These results suggest that labelling CAR-T cells with GVs does not compromise their intrinsic tumour-killing capabilities.

Beyond their direct cytotoxic effects, CAR-T cells also contribute to anti-tumour immunity by producing cytokines and inducing immune reactions.[51] Among these cytokines, interferon-gamma (IFN-γ) is a critical mediator of the immune response.[52] Our Enzyme-Linked Immunosorbent Assay (ELISA) results demonstrated that both CAR-T and GVs@CAR-T cells released substantial amounts of IFN-γ upon co-culture with Raji-Luc cells, with concentrations increasing by 86.0- and 85.7-fold, respectively, compared to CAR-T cells not co-cultured with tumour cells (Figure 3C). Similarly, the release of TNF-α, IL-2, and IL-10 was significantly elevated in CAR-T and GVs@CAR-T cells co-cultured with Raji-Luc cells compared to non-co-cultured CAR-T cells. These findings underscore the preserved immunomodulatory function of GVs@CAR-T cells. Moreover, the expression of key T-cell activation (CD69) and exhaustion (PD-1) markers was comparable between GV-labelled and unlabelled CAR-T cells (Figure 3D). This observation further supports the conclusion that GVs labelling does not adversely affect the functional properties of CAR-T cells. Collectively, these in vitro results demonstrated that GVs@CAR-T cells retained their tumour-killing capacity and immunomodulatory functions, making them suitable candidates for in vivo tracking via CEUS imaging.

To translate these findings into an in vivo setting, we used CEUS to monitor the dynamic trafficking and tumour-homing behaviour of GVs@CAR-T cells after adoptive transfer (Figure 3E). Non-labelled CAR-T cells exhibited no significant changes in imaging scans at any post-transfer time point (Figure 3F). In contrast, GVs@CAR-T cells displayed clear spot-like enhancements immediately after infusion, with the CEUS signal intensity peaking at 48 h before gradually declining (Supplementary Figure 7). Ex vivo fluorescence imaging performed 48 h post-infusion revealed strong fluorescence signals in the tumour tissues of mice infused with GVs@CAR-T cells (Figure 3G). These results align with previously reported patterns of CAR-T cell accumulation at this time point,[53] confirming the effective tumour-homing ability of GVs@CAR-T cells.

In summary, this section provides a comprehensive evaluation of the tumour-killing function and in vivo behaviour of GVs@CAR-T cells. By combining functional assays and non-invasive imaging techniques, we demonstrated that GVs labelling does not compromise CAR-T cell functionality while enabling real-time monitoring of their trafficking and tumour-homing dynamics. This versatile and readily accessible imaging technique could significantly enhance the practical implementation and administration of CAR-T cells. However, further studies are required to investigate the long-term persistence and therapeutic outcomes of GVs@CAR-T cells in preclinical models.

Antigen-Specific Homing and Therapeutic Efficacy Validation of GVs@CAR-T

The Enhanced Permeability and Retention (EPR) effect in tumour tissues is a well-documented phenomenon that contributes to drug retention and serves as a nonspecific passive targeting mechanism.[54,55] However, this effect may also lead to the nonspecific infiltration of GVs@CAR-T cells at the tumour site, raising questions regarding whether the observed imaging signals reflect specific targeting or nonspecific accumulation. To address this critical issue, we designed two xenograft treatment animal models (CD19+ and CD19-) to evaluate the specificity of GVs@CAR-T infiltration at the tumour site (Figure 4A).

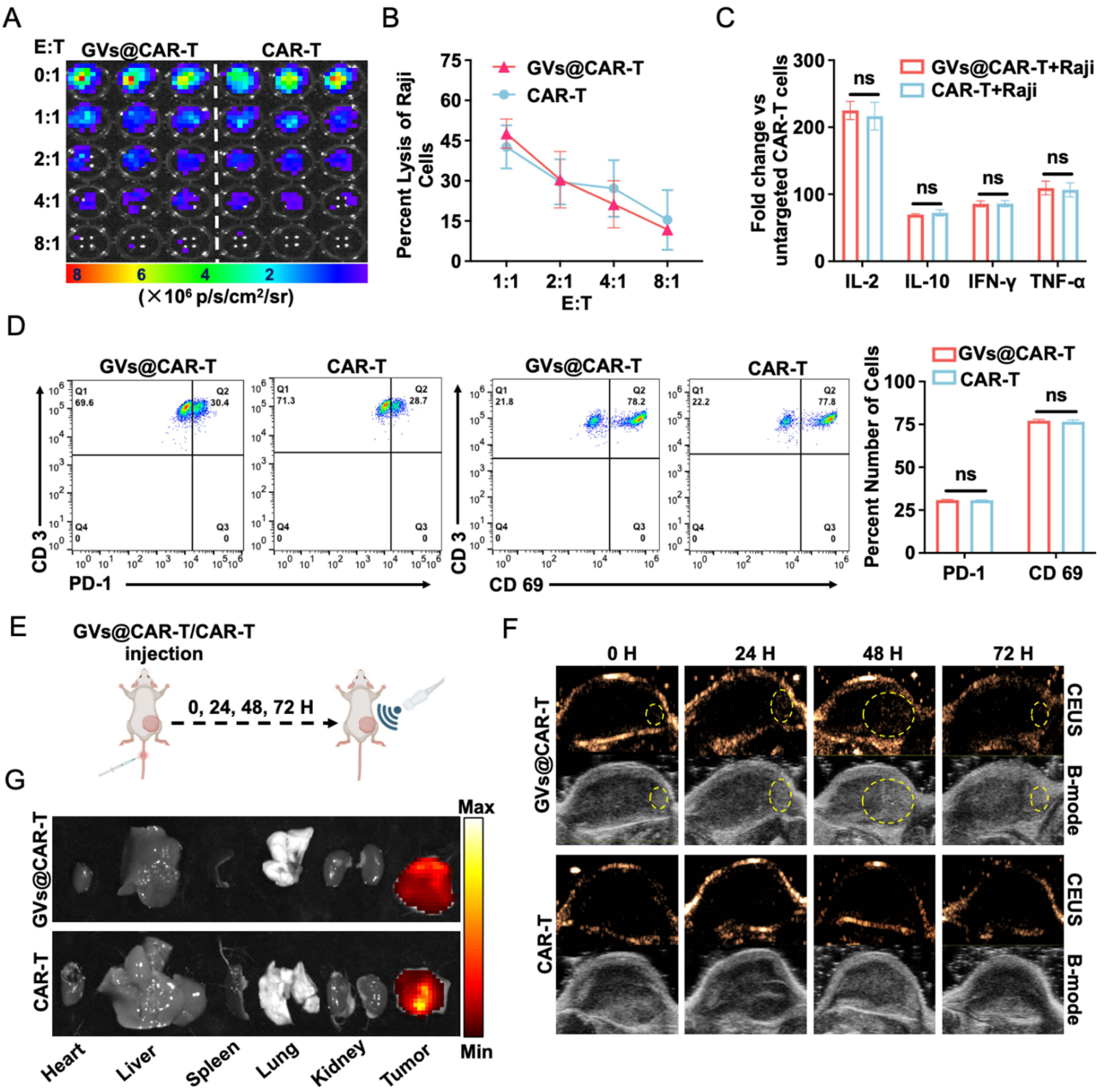

Figure 3 Anti-tumour activity of GVs@CAR-T cells In vitro and In vivo ultrasound imaging. (**A**) BLI cytotoxicity assay showing the viability of Raji-Luc cells in the presence of CAR-T cells or GVs@CAR-T cells at increasing effector-to-target (E:T) ratios. (**B**) The lysis of CAR-T and GVs@CAR-T cells on Raji cells under different effector-to-target (E:T) ratios was evaluated using the LDH release assay (n=3). (**C**) Fold change of expression of various cytokines by CAR-T or GVs@CAR-T cells, normalized to untargeted CAR-T cells (n=3). (**D**) Relative number of GVs@CAR-T and CAR-T cells that express exhaustion and activation markers (n=3). (**E**) Ultrasound imaging schematic. (**F**) Intravenous injection of GVs@CAR-T (n=3) or CAR-T (n=3) at various time points CEUS imaging (upper) and B-mode imaging (lower). Yellow circles denote the region of GVs@CAR-T. (**G**) Representative ex vivo IVIS images of major organs and tumours collected at 48 hours after the treatment (n=3). Positive fluorescence indicates the presence of adoptive CAR-T cells. ns, not significant.

The results demonstrated that the CEUS imaging signal intensity of GVs@CAR-T at the tumour sites in the CD19+ models was significantly higher than in the CD19- models at the same time point post-administration (Figure 4B). Notably, the CD19- models exhibited negligible signal intensity at the tumour site (Figure 4D), which contradicted the expectations based on the EPR effect. This discrepancy may be attributed to the detection threshold of CEUS imaging, which is approximately 5×10^5 cells/mL. At this threshold, nonspecific infiltration of GVs@CAR-T in CD19- models could not be visualised through CEUS imaging. These findings confirm that the proposed visualisation strategy is capable

https://doi.org/10.2147/IJN.S508846

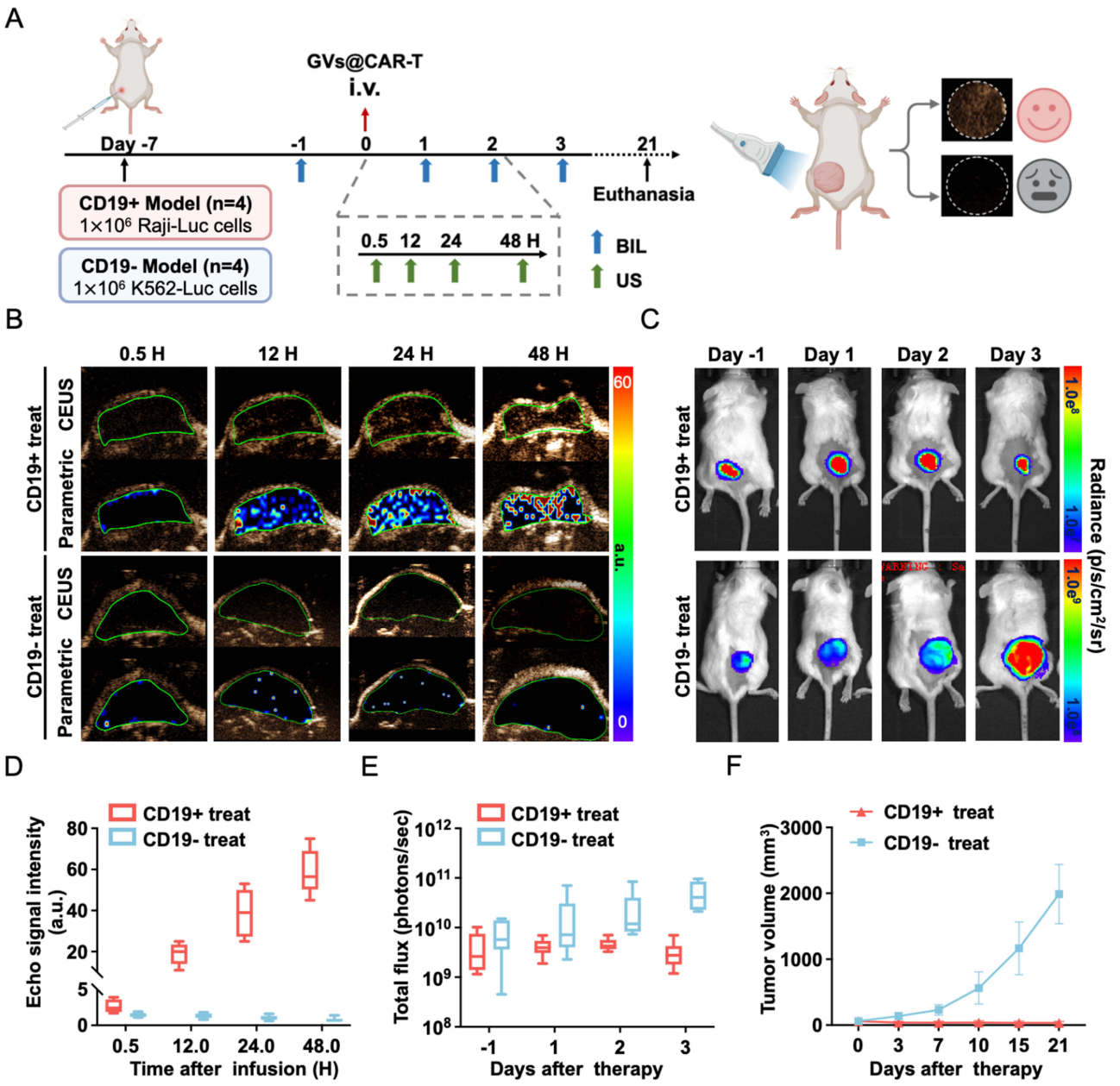

Figure 4 In vivo targeted tracking of GVs@CAR-T Cells and efficacy evaluation. (**A**) The schematic graph of the experimental design. (**B**) Representative ultrasound images of post-injections GVs@CAR-T in CD19-positive/negative models, at 0.5, 12, 24 and 48 h, including CEUS imaging (upper) and parametric imaging (lower). (**C**) Representative BLI imaging of CD19-positive/negative models on days 1 pre-treatment and 1, 2, and 3 post-treatment with GVs@CAR-T cells. (**D**) Quantified CEUS intensity of GVs@CAR-T in CD19-positive/negative models. (**E**) Quantified BLI intensity of CD19-positive/negative model tumours. (**F**) Tumour volume.

of distinguishing the specific targeted homing of CAR-T cells to tumours from nonspecific accumulation, thereby validating its utility for monitoring CAR-T cell behaviour in vivo.

To further investigate the anti-tumour efficacy of GVs@CAR-T in both models, we monitored tumour growth and therapeutic responses using BLI (Figure 4C and E) and tumour volume measurements (Figure 4F). In the CD19+ models, BLI intensity at the tumour site decreased post-treatment compared to pre-treatment levels, and tumour volumes decreased. In contrast, the CD19- models exhibited increased fluorescence intensity and tumour volume growth, indicating that GVs@CAR-T therapy was ineffective in the absence of specific targeting.

In summary, this section demonstrates that CEUS imaging can serve as a powerful tool for monitoring the specific targeted homing of CAR-T cells to tumours, distinguishing it from nonspecific accumulation mediated by the EPR effect.

These findings highlight the importance of specific CAR-T-cell infiltration for achieving therapeutic efficacy and provide valuable insights into the development of noninvasive imaging strategies for monitoring CAR-T-cell therapy in clinical settings. However, further research is needed to fully understand the relationship between early CAR-T-cell infiltration and therapeutic outcomes, as well as to optimise imaging techniques for broader applications.

Therapeutic Efficacy Be Predicted Based on Early Intra-Tumoral GVs@CAR-T Cell Infiltration

To further evaluate the relationship between GVs@CAR-T cell-specific infiltration at the tumour site and therapeutic efficacy, we performed CD19+ xenograft animal model experiments as show in Figure 5A. In tumour-bearing mice, the BLI signal intensity at the tumour site varied among different mice at the same time point after treatment in the GVs@CAR-T group (Figure 5B). Further observation of GVs@CAR-T CEUS imaging of the tumour site revealed that at 48 h post-administration, the stronger the CEUS signal of GVs@CAR-T at the tumour site in tumour-bearing mice (Figure 5C), the lower the fluorescence intensity detected at the tumour site at 72 h post-administration (Figure 5D). Immunofluorescence staining of CD3+ in the tumour tissue was conducted to evaluate the persistence of GVs@CAR-T cells in the tumour microenvironment (TME). As shown in Supplementary Figure 8, treatment with GVs@CAR-T resulted in a marked increase in CD3+ cell density within tumours compared to mock-T at all assessed time points. These experiments provide evidence of GVs@CAR-T cell infiltration and retention at the tumour site, supporting the notion that GVs@CAR-T cells maintain their presence in the

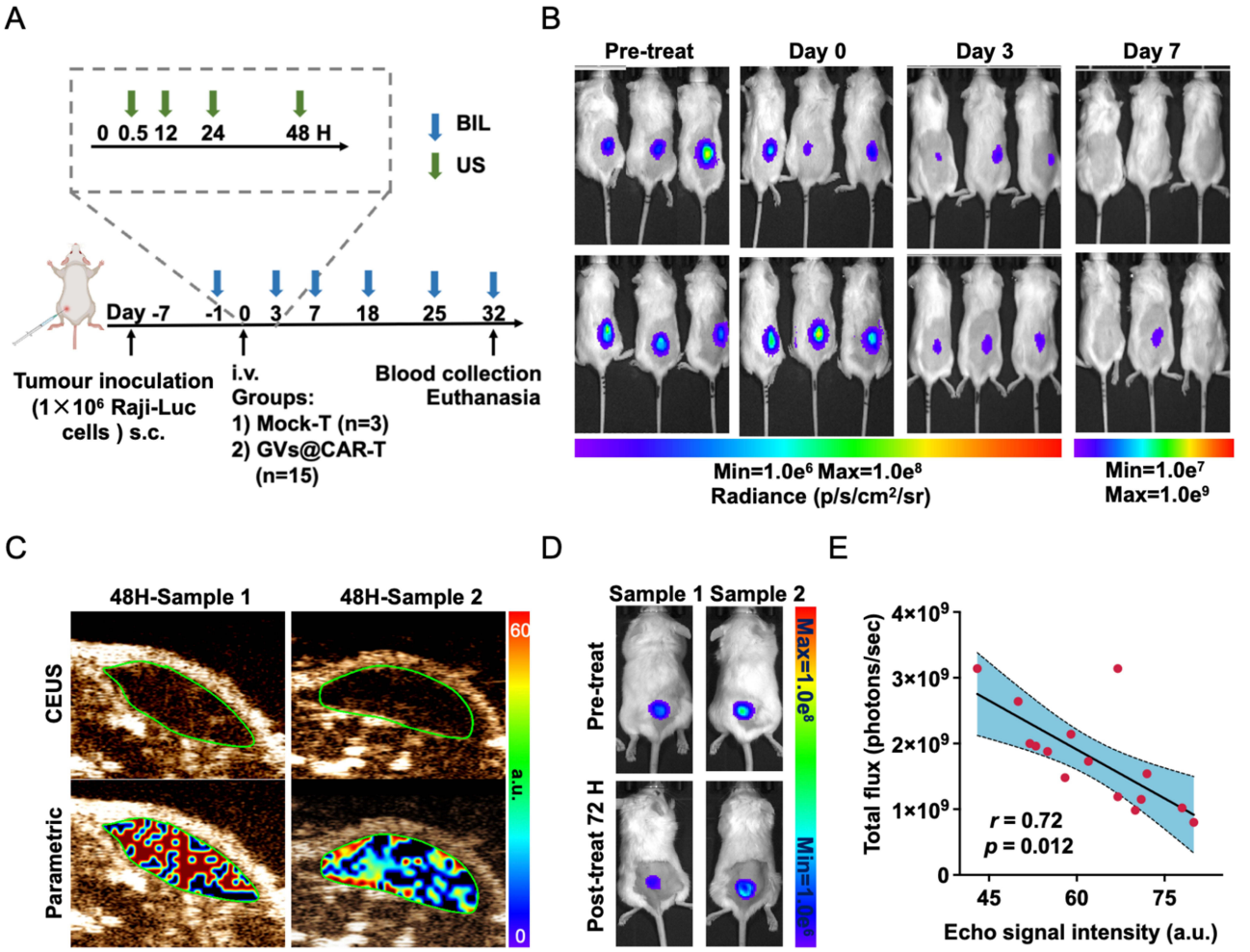

Figure 5 The early intra-tumoral GVs@CAR-T cell infiltration predicted tumor response. (**A**) The schematic graph of the experimental design. (**B**) Representative of the whole-body BLI of Raji-Luc-bearing mice in the treatment group. (**C**) Representative ultrasound images and (**D**) BLI in CD19-positive tumours. (**E**) Correlation analysis.

https://doi.org/10.2147/IJN.S508846

tumour tissue over time. We conducted Pearson correlation analysis to evaluate the relationship between the CEUS signal intensity of GVs@CAR-T at the tumour site 48 h after administration and the tumour BLI intensity 72 h after administration in tumour-bearing mice. The analysis revealed a strong significant negative correlation between the early CEUS signal intensity of GVs@CAR-T and the BLI intensity of the tumour (Figure 5E). These findings further suggest that early ultrasound imaging tracking of GVs@CAR-T at the tumour site can preliminarily predict therapeutic efficacy.

Meanwhile, no evidence of systemic toxicity was observed in mice treated with GVs@CAR-T injection (Supplementary Figure 9) and the body weights (Supplementary Figure 10) of mice were not significantly changed in any case, which further supports the safety profile of this approach.

This approach can provide valuable insights into the early assessment of treatment responses and guide personalised therapeutic strategies in clinical settings. Our findings highlight the potential of GVs@CAR-T cell-based ultrasound imaging as a predictive tool for therapeutic efficacy. This study had several limitations. First, the sample size of the animal model experiments was relatively small, which may have limited the statistical power of the analysis. Second, although our findings demonstrate a strong correlation between GVs@CAR-T accumulation and therapeutic efficacy, the underlying mechanisms remain to be fully elucidated. Further studies are required to validate these findings in larger animal models and clinical trials.

Conclusion

In conclusion, this study established CEUS imaging as a non-invasive platform for real-time monitoring of GVs@CAR-T cell dynamics. We were able to predict the therapeutic effect based on the infiltration of GVs@CAR-T cells into early tumours and provide indications for the design and optimisation of related therapeutic strategies for cart cell therapy. While excelling in temporal resolution, the current limitations include tissue penetration depth and semi-quantitative analysis. Future developments should integrate multimodal validation and advanced clinical trials to ultimately enable image-guided precision immunotherapy.

Acknowledgments

The authors are grateful for the funding provided for this study by the National Natural Science Foundation of China (82102051, 82071927, 82202166), Guangzhou Science and Technology Program (202002030104, 2024A03J0993, 2023A03J0281, 2025A03J4358), Talents' plan Foundation of Guangdong Second Provincial General Hospital (2024E003, 2024E006, 2024F002).

Author Contributions

Liu and Liu designed and supported the project. Y. He provided suggestions for the project design and article writing. Y. Huang and Z. Yin performed the experiments, collected data, and wrote the original draft. R. Xu analysed and interpreted the data and reviewed and edited the original draft. Q. Zhang and M. Zhou provided support in writing and editing the original draft. Z. Xu and W. Zheng supported the data curation and methodology. All authors made a significant contribution to the work reported, whether that is in the conception, study design, execution, acquisition of data, analysis and interpretation, or in all these areas; took part in drafting, revising or critically reviewing the article; gave final approval of the version to be published; have agreed on the journal to which the article has been submitted; and agree to be accountable for all aspects of the work.

Disclosure

The authors declare no conflicts of interest in this work.

References

1. Xue Y, Che J, Ji X, Li Y, Xie J, Chen X. Recent advances in biomaterial-boosted adoptive cell therapy. *Chem Soc Rev*. 2022;51(5):1766–1794. doi:10.1039/d1cs00786f
2. Pan K, Farrukh H, Chittepu V, Xu H, Pan CX, Zhu Z. CAR race to cancer immunotherapy: from CAR T, CAR NK to CAR macrophage therapy. *J Exp Clin Cancer Res*. 2022;41(1):119. doi:10.1186/s13046-022-02327-z

3. Chen Y, Yu Z, Tan X, et al. CAR-macrophage: a new immunotherapy candidate against solid tumors. *Biomed Pharmacother*. 2021;139:111605. doi:10.1016/j.biopha.2021.111605
4. Sterner RC, Sterner RM. CAR-T cell therapy: current limitations and potential strategies. *Blood Cancer J*. 2021;11(4):69. doi:10.1038/s41408-021-00459-7
5. Ma S, Li X, Wang X, et al. Current Progress in CAR-T Cell Therapy for Solid Tumors. *Int J Biol Sci*. 2019;15(12):2548–2560. doi:10.7150/ijbs.34213
6. Singh AK, McGuirk JP. CAR T cells: continuation in a revolution of immunotherapy. *Lancet Oncol*. 2020;21(3):e168–e178. doi:10.1016/s1470-2045(19)30823-x
7. Maalej KM, Merhi M, Inchakalody VP, et al. CAR-cell therapy in the era of solid tumor treatment: current challenges and emerging therapeutic advances. *mol Cancer*. 2023;22(1):20. doi:10.1186/s12943-023-01723-z
8. Ali S, Kjeken R, Niederlaender C, et al. The European Medicines Agency Review of Kymriah (Tisagenlecleucel) for the Treatment of Acute Lymphoblastic Leukemia and Diffuse Large B-Cell Lymphoma. *Oncologist*. 2020;25(2):e321–e327. doi:10.1634/theoncologist.2019-0233
9. Maude SL, Frey N, Shaw PA, et al. Chimeric antigen receptor T cells for sustained remissions in leukemia. *N Engl J Med*. 2014;371(16):1507–1517. doi:10.1056/NEJMoa1407222
10. Zhang P, Zhang G, Wan X. Challenges and new technologies in adoptive cell therapy. *J Hematol Oncol*. 2023;16(1):97. doi:10.1186/s13045-023-01492-8
11. Martinez M, Moon EK. CAR T Cells for Solid Tumors: new Strategies for Finding, Infiltrating, and Surviving in the Tumor Microenvironment. *Front Immunol*. 2019;10:128. doi:10.3389/fimmu.2019.00128
12. Dey M, Kim MH, Dogan M, et al. Chemotherapeutics and CAR-T Cell-Based Immunotherapeutics Screening on a 3D Bioprinted Vascularized Breast Tumor Model. *Adv Funct Mater*. 2022;32(52):3966. doi:10.1002/adfm.202203966
13. Chohan KL, Siegler EL, Kenderian SS. CAR-T Cell Therapy: the Efficacy and Toxicity Balance. *Curr Hematol Malig Rep*. 2023;18(2):9–18. doi:10.1007/s11899-023-00687-7
14. Huang W, Li J, Liao MZ, et al. Clinical Pharmacology Perspectives for Adoptive Cell Therapies in Oncology. *Clin Pharmacol Ther*. 2022;112(5):968–981. doi:10.1002/cpt.2509
15. Qi T, McGrath K, Ranganathan R, Dotti G, Cao Y. Cellular kinetics: a clinical and computational review of CAR-T cell pharmacology. *Adv Drug Deliv Rev*. 2022;188:114421. doi:10.1016/j.addr.2022.114421
16. Liu C, Ayyar VS, Zheng X, et al. Model-Based Cellular Kinetic Analysis of Chimeric Antigen Receptor-T Cells in Humans. *Clin Pharmacol Ther*. 2021;109(3):716–727. doi:10.1002/cpt.2040
17. Abramson JS. Anti-CD19 CAR T-Cell Therapy for B-Cell Non-Hodgkin Lymphoma. *Transfus Med Rev*. 2020;34(1):29–33. doi:10.1016/j.tmrv.2019.08.003
18. Deng C, Zheng M, Han S, et al. GSH-activated Porphyrin Sonosensitizer Prodrug for Fluorescence Imaging-guided Cancer Sonodynamic Therapy. *Adv Funct Mater*. 2023;33(32):348. doi:10.1002/adfm.202300348
19. Lai Benjamin FL, Lu Rick X, Hu Y, et al. Recapitulating pancreatic tumor microenvironment through synergistic use of patient organoids and organ-on-a-chip vasculature. *Adv Funct Mater*. 2020;30(48):545. doi:10.1002/adfm.202000545
20. Bulte JWM, Wang C, Shakeri-Zadeh A. In vivo Cellular Magnetic Imaging: labeled vs. Unlabeled Cells. *Adv Funct Mater*. 2022;32(50):7626. doi:10.1002/adfm.202207626
21. Koshkina O, Lajoinie G, Bombelli FB, et al. Multicore Liquid Perfluorocarbon-Loaded Multimodal Nanoparticles for Stable Ultrasound and (19)F MRI Applied to In vivo Cell Tracking. *Adv Funct Mater*. 2019;29(19):6485. doi:10.1002/adfm.201806485
22. Kurtz K, Eibler L, Dacek MM, et al. Engineering CAR-T cells for radiohapten capture in imaging and radioimmunotherapy applications. *Theranostics*. 2023;13(15):5469–5482. doi:10.7150/thno.87489
23. Scott JI, Gutkin S, Green O, et al. A Functional Chemiluminescent Probe for In vivo Imaging of Natural Killer Cell Activity Against Tumours. *Angew Chem Int Ed Engl*. 2021;60(11):5699–5703. doi:10.1002/anie.202011429
24. Kiru L, Zlitni A, Tousley AM, et al. In vivo imaging of nanoparticle-labeled CAR T cells. *Proc Natl Acad Sci U S A*. 2022;119(6). doi:10.1073/pnas.2102363119
25. Wu WE, Chang E, Jin L, et al. Multimodal In vivo Tracking of Chimeric Antigen Receptor T Cells in Preclinical Glioblastoma Models. *Invest Radiol*. 2023;58(6):388–395. doi:10.1097/rli.0000000000000946
26. Yu EY, Chandrasekharan P, Berzon R, et al. Magnetic Particle Imaging for Highly Sensitive, Quantitative, and Safe In vivo Gut Bleed Detection in a Murine Model. *ACS Nano*. 2017;11(12):12067–12076. doi:10.1021/acsnano.7b04844
27. Weist MR, Starr R, Aguilar B, et al. PET of Adoptively Transferred Chimeric Antigen Receptor T Cells with (89)Zr-Oxine. *J Nucl Med*. 2018;59(10):1531–1537. doi:10.2967/jnumed.117.206714
28. Ferreira CA, Ni D, Rosenkrans ZT, Cai W. Radionuclide-Activated Nanomaterials and Their Biomedical Applications. *Angew Chem Int Ed Engl*. 2019;58(38):13232–13252. doi:10.1002/anie.201900594
29. Rama E, Mohapatra SR, Melcher C, et al. Monitoring the Remodeling of Biohybrid Tissue-Engineered Vascular Grafts by Multimodal Molecular Imaging. *Adv Sci (Weinh)*. 2022;9(10):e2105783. doi:10.1002/advs.202105783
30. Wang J, Wang Y, Zhong L, Yan F, Zheng H. Nanoscale contrast agents: a promising tool for ultrasound imaging and therapy. *Adv Drug Deliv Rev*. 2024;207:115200. doi:10.1016/j.addr.2024.115200
31. Yuan Y, Xu M, Ren Y, He L, Chen J, Sun L. Clinical Value of Contrast-Enhanced Ultrasound in Breast Cancer Diagnosis. *Comput Math Methods Med*. 2022;2022:2017026. doi:10.1155/2022/2017026
32. Ingels A, Leguerney I, Cournède PH, et al. Ultrasound Molecular Imaging of Renal Cell Carcinoma: VEGFR targeted therapy monitored with VEGFR1 and FSHR targeted microbubbles. *Sci Rep*. 2020;10(1):7308. doi:10.1038/s41598-020-64433-2
33. Otani K, Nishimura H, Kamiya A, Harada-Shiba M. Simplified Preparation of α(v)β(3) Integrin-Targeted Microbubbles Based on a Clinically Available Ultrasound Contrast Agent: validation in a Tumor-Bearing Mouse Model. *Ultrasound Med Biol*. 2018;44(5):1063–1073. doi:10.1016/j.ultrasmedbio.2018.01.017
34. Cai X, Yang F, Gu N. Applications of magnetic microbubbles for theranostics. *Theranostics*. 2012;2(1):103–112. doi:10.7150/thno.3464
35. Lin Q, Choyke PL, Sato N. Visualizing vasculature and its response to therapy in the tumor microenvironment. *Theranostics*. 2023;13(15):5223–5246. doi:10.7150/thno.84947

36. Sheth V, Wang L, Bhattacharya R, Mukherjee P, Wilhelm S. Strategies for Delivering Nanoparticles across Tumor Blood Vessels. *Adv Funct Mater*. 2021;31(8). doi:10.1002/adfm.202007363
37. Zhang S, Deng G, Liu F, et al. Autocatalytic Delivery of Brain Tumor-targeting, Size-shrinkable Nanoparticles for Treatment of Breast Cancer Brain Metastases. *Adv Funct Mater*. 2020;30(14). doi:10.1002/adfm.201910651
38. Xu Z, Liu H, Tian H, Yan F. Real-Time Imaging Tracking of Engineered Macrophages as Ultrasound-Triggered Cell Bombs for Cancer Treatment. *Adv. Funct. Mater.* 2020;30(14):1910304.
39. Gong Z, He Y, Zhou M, et al. Ultrasound imaging tracking of mesenchymal stem cells intracellularly labeled with biosynthetic gas vesicles for treatment of rheumatoid arthritis. *Theranostics*. 2022;12(5):2370–2382. doi:10.7150/thno.66905
40. Shapiro MG, Goodwill PW, Neogy A, et al. Biogenic gas nanostructures as ultrasonic molecular reporters. *Nat Nanotechnol*. 2014;9(4):311–316. doi:10.1038/nnano.2014.32
41. Hao Y, Li Z, Luo J, Li L, Yan F. Ultrasound Molecular Imaging of Epithelial Mesenchymal Transition for Evaluating Tumor Metastatic Potential via Targeted Biosynthetic Gas Vesicles. *Small*. 2023;19(21):e2207940. doi:10.1002/smll.202207940
42. Lakshmanan A, Lu GJ, Farhadi A, et al. Preparation of biogenic gas vesicle nanostructures for use as contrast agents for ultrasound and MRI. *Nat Protoc*. 2017;12(10):2050–2080. doi:10.1038/nprot.2017.081
43. Jiang Y, Hou X, Zhao X, Jing J, Sun L. Tracking adoptive natural killer cells via ultrasound imaging assisted with nanobubbles. *Acta Biomater*. 2023;169:542–555. doi:10.1016/j.actbio.2023.07.058
44. Lu J, Jiang G. The journey of CAR-T therapy in hematological malignancies. *mol Cancer*. 2022;21(1):194. doi:10.1186/s12943-022-01663-0
45. Wang G, Song L, Hou X, et al. Surface-modified GVs as nanosized contrast agents for molecular ultrasound imaging of tumor. *Biomaterials*. 2020;236:119803. doi:10.1016/j.biomaterials.2020.119803
46. Zlitni A, Gambhir SS. Molecular imaging agents for ultrasound. *Curr Opin Chem Biol*. 2018;45:113–120. doi:10.1016/j.cbpa.2018.03.017
47. Dai H, Wu Z, Jia H, et al. Bispecific CAR-T cells targeting both CD19 and CD22 for therapy of adults with relapsed or refractory B cell acute lymphoblastic leukemia. *J Hematol Oncol*. 2020;13(1):30. doi:10.1186/s13045-020-00856-8
48. Xie L, Wang J, Song L, Jiang T, Yan F. Cell-cycle dependent nuclear gene delivery enhances the effects of E-cadherin against tumor invasion and metastasis. *Signal Transduct Target Ther*. 2023;8(1):182. doi:10.1038/s41392-023-01398-4
49. Minn I, Huss DJ, Ahn HH, et al. Imaging CAR T cell therapy with PSMA-targeted positron emission tomography. *Sci Adv*. 2019;5(7):eaaw5096. doi:10.1126/sciadv.aaw5096
50. Jogalekar MP, Rajendran RL, Khan F, Dmello C, Gangadaran P, Ahn BC. CAR T-Cell-Based gene therapy for cancers: new perspectives, challenges, and clinical developments. *Front Immunol*. 2022;13:925985. doi:10.3389/fimmu.2022.925985
51. Dong C. Cytokine Regulation and Function in T Cells. *Annu Rev Immunol*. 2021;39:51–76. doi:10.1146/annurev-immunol-061020-053702
52. Ivashkiv LB. IFNγ: signalling, epigenetics and roles in immunity, metabolism, disease and cancer immunotherapy. *Nat Rev Immunol*. 2018;18(9):545–558. doi:10.1038/s41577-018-0029-z
53. Wang XY, Wang Y, Wu Q, et al. Feasibility study of (68)Ga-labeled CAR T cells for in vivo tracking using micro-positron emission tomography imaging. *Acta Pharmacol Sin*. 2021;42(5):824–831. doi:10.1038/s41401-020-00511-5
54. Biancacci I, De Lorenzi F, Theek B, et al. Monitoring EPR Effect Dynamics during Nanotaxane Treatment with Theranostic Polymeric Micelles. *Adv Sci (Weinh)*. 2022;9(10):e2103745. doi:10.1002/advs.202103745
55. Cheng Z, Li M, Dey R, Chen Y. Nanomaterials for cancer therapy: current progress and perspectives. *J Hematol Oncol*. 2021;14(1):85. doi:10.1186/s13045-021-01096-0